2018-01-0721 Published 03 Apr 2018

Combined Drag and Cooling Optimization of a Car Vehicle with an Adjoint-Based Approach

Guillaume Pierrot and Jacques Papper ICON Technology and Process Consulting

Taeyoung Han and Shailendra Kaushik General Motors LLC

Citation: Pierrot, G., Papper, J., Han, T., and Kaushik, S., "Combined Drag and Cooling Optimization of a Car Vehicle with an Adjoint-Based Approach," SAE Technical Paper 2018-01-0721, 2018, doi:10.4271/2018-01-0721.

Abstract

The main objective of this work is to present an adjoint-based methodology to address combined optimization of drag force and cooling flow rate of an industrial vehicle. In order to cope with cooling effect, the *volumetric flow rate* is treated through a newly introduced cost function and the corresponding adjoint source term is derived. Also an alternative strategy is presented to tackle aerodynamic vehicle design improvement that relies on a so-called *indirect force computation*. The overall optimization is treated as a Multi-Objective problem and an original approach, called *Optimize Both Favor One (OBFO)*, is introduced that allows selective emphasis on one or another objective without resorting to artificial cost function balancing. Finally, comparative results are presented to demonstrate the merit of the proposed methodology.

Introduction

Car vehicles design improvement through adjoint-driven shape optimization has grown in popularity over the past 10 years as robust methodologies and versatile software tools started to emerge. The most appealing feature of this technology, which is to compute sensitivity fields at a cost nearly independent of the number of design parameters, makes it a must have when addressing intensive design exploration campaigns.

In [14], by example, it is emphasized how powerful a tool adjoint-based optimization is for ducted flow applications, such as airducts for cabin ventilation or engine intake ports. Also it is reported to have matured enough over the past few years to allow a systematic usage for various automotive applications.

The question of finding some optimal trade-off in between multiple objectives, however, especially if they appear to be somewhat contradictory is still a challenging issue.

When it comes to car external aerodynamics, typically, a few parameters come to consideration such as shape, frontal area, operating speed, and cooling drag. Even for the most basic air cooled system architecture, a radiator is the essential component in charge of taking the heat away from the coolant liquid circulating through it.

In the automotive industry the manufacturer has to compromise these key parameters with design, weight, space or cost of manufacture problematics.

It is easy to modify the external shape of a car, however the small space available in an under-hood compartment - driven by increasing compacity requirements - makes it very complex to optimize the cooling system (see Figure 1).

The challenge of accomplishing simultaneous objectives of drag reduction and cooling flow rate increase are currently done by iterations between the aerodynamics departments and front-end airflow departments in most automotive OEMs. In some rare instances, expensive design of experiment approaches are taken. As an alternative, the authors have been looking into applying multi-objectives adjoint method optimization on a production car with complex under-hood.

All of the numerical results presented in this paper were obtained with the iconCFD® [1] supported CFD process.

Modeling

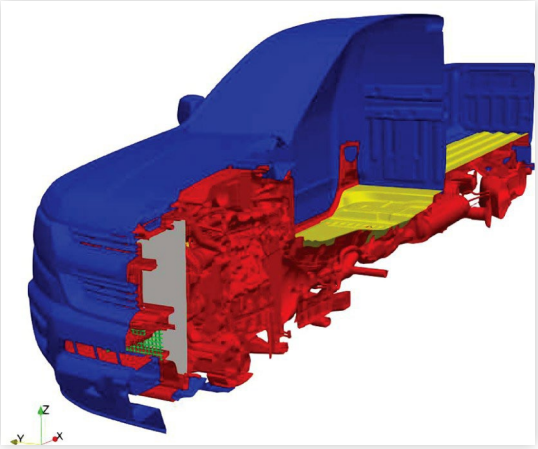
As a simplified representation of the problem we'll consider the configuration presented in Figure 2 where some aerodynamic bodies are disseminated all along the flow and some prescribed internal zone H_X represents the heat exchanger. The goal is to control the flow rate through H_X (hence the cooling effect) whilst driving the drag as low as possible for better aerodynamic efficiency. The heat exchanger action is modeled through a generic anisotropic Darcy-Forchheimer law (see [2] for reference):

$$(\nabla p)_{porous} = \left(\overline{\overline{A}} + \|\boldsymbol{u}\| \overline{\overline{B}}\right)\boldsymbol{u} \tag{1}$$

Where $\overline{\overline{A}}\,\boldsymbol{u}$ is the so-called Darcy term whereas $\|\boldsymbol{u}\|\,\overline{\overline{B}}\,\boldsymbol{u}$ is the Forchheimer term.

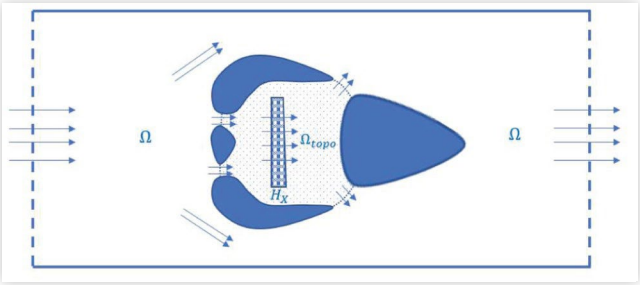
© 2018 SAE International; General Motors LLC.

FIGURE 1 Typical underhood of a pick-up truck vehicle. The heat exchanger is represented in grey in front of the engine block.



© SAE International

FIGURE 2 Schematic representation with arbitrary aerodynamic bodies (blue solid): goal is to increase the flow rate through the heat exchanger H_X whilst keeping the drag as low as possible. The dashed area Ω_{topo} represents the region to optimize.



© SAE International

Flow Equations

One shall consider Reynolds-Averaged Navier-Stokes equations in incompressible regime augmented with the aforementioned porous media source term:

$$\mathbb{R}_u = \nabla.\left(\boldsymbol{u}\otimes\boldsymbol{u}\right)+\nabla\cdot\left(-\left(\nu+\nu_t\right)\left(\nabla\boldsymbol{u}+\nabla^T\boldsymbol{u}\right)\right) + \nabla \mathrm{p}+\left(\nabla p\right)_{porous}\ \mathbf{1}_{H_X}=\mathbf{0} \tag{2}$$

$$\mathbb{R}_p = \nabla.\boldsymbol{u}=0 \tag{3}$$

$$\mathbb{R}_z = \text{convection}+\text{diffusion}+\text{dissipation} + \text{production}=0 \tag{4}$$

$$\mathbb{R}_{\nu_t} = \nu_t - g\left(z\right)=0 \tag{5}$$

Where u and p denote respectively the flow velocity and pressure and $\boldsymbol{\nu}$ and $\boldsymbol{\nu_t}$ the kinematic and turbulent viscosity. The indicator function for $\boldsymbol{H_X}$ is $\mathbf{1}_{\boldsymbol{HX}}$ and R_z is meant to be any turbulence model with z denoting the generic turbulent variables vector. Finally, this system of equations is supplemented with appropriate boundary conditions at the inlet, outlet and the surface of aerodynamic bodies.

Adjoint Equations

When it comes to adjoint solver, 2 main approaches coexist, namely *discrete* and *continuous* methodologies. In the first approach, the differentiation step happens *after* the equations discretization, guaranteeing a full consistency with the primal solver, while in the second one it happens *before*, at the continuous level, and the obtained adjoint equations are then further discretized and solved, using any reasonable CFD solver (usually the primal solver machinery is recycled). They both have their pros and cons and it goes far beyond the scope of this paper to compare their merits, but the interested reader can refer to [4] for a detailed discussion. Here it is enough to say that finding an acceptable compromise between CPU efficiency and memory consumption is still a challenging issue for the *discrete* approach when addressing industrial scaled CFD problems and that for this reason, despite its own challenges, the *continuous adjoint* approach is still the method of choice for this class of problems.

The derivation of incompressible Navier-Stokes adjoint equations has been carried out rigorously by several authors (see eg. [2]). When it comes to RANS equations however, the derivation of turbulence models adds some significant complexity and, although some authors have proposed adjoint counterparts of most popular turbulence models (see eg [5]) the so-called *frozen turbulence* assumption is still widely used in practice, suggesting to neglect the effects on the mean flow of the turbulent viscosity modifications induced by the design change. As a result, in the absence of source terms in the primal, the adjoint equations read (see [6] for details):

$$\mathbb{R}_{u^*} = -\nabla.\left(\boldsymbol{u}^*\otimes\boldsymbol{u}\right)+\nabla\cdot\left(-\left(\nu+\nu_t\right)\left(\nabla\boldsymbol{u}^*+\nabla^T\boldsymbol{u}^*\right)\right) + \nabla \mathrm{p}^*+\underbrace{\left(\nabla\boldsymbol{u}\right)\ \boldsymbol{u}^*}_{ATC-0}+\left(\frac{\partial \boldsymbol{g}}{\partial \boldsymbol{u}}\right)^T=\mathbf{0} \tag{6}$$

$$\mathbb{R}_{p^*} = \nabla\cdot\boldsymbol{u}^*-\left(\frac{\partial g}{\partial p}\right)^T=0 \tag{7}$$

Where $\boldsymbol{u}^*$ and $\mathbf{p}^*$ denote the adjoint velocity and pressure, respectively, $\boldsymbol{g}$ is the cost function volumetric integrand:

$$F=\int_{\Omega} g\left(\boldsymbol{u},p\right)+\int_{\partial\Omega} f \tag{8}$$

$$\text{And, by convention}: \nabla\boldsymbol{u}=\left(\frac{\partial \boldsymbol{u}_\beta}{\partial \boldsymbol{x}_\alpha}\right)_{1\le\alpha\le3}^{1\le\beta\le3} \quad \left(\alpha \text{ is the row index}\right) \tag{9}$$

If in addition, the following shape is assumed for the boundary integrand f:

$$\left.\begin{aligned} f &\equiv f\left(u,\tau_n\right)\\ \tau_n &= p\,\boldsymbol{n}-\left(\nu+\nu_t\right)\left(\nabla\boldsymbol{u}+\nabla^T\boldsymbol{u}\right)\boldsymbol{n}\end{aligned}\right\} \tag{10}$$

© 2018 SAE International; General Motors LLC.

With $\boldsymbol{n}$ being the exterior normal, then the appropriate boundary conditions for (6)-(7) read:

$$\left.\begin{aligned}\textbf{outlet}: \tau_n^* &= u^*\left(u\cdot n\right)+\left(\frac{\partial \mathrm{f}}{\partial \mathbf{u}}\right)^T \\ \textbf{inlet}+\textbf{walls}: u^* &= -\left(\frac{\partial \mathrm{f}}{\partial \tau_{\mathrm{n}}}\right)^T\end{aligned}\right\} \tag{11}$$

The so-called *ATC* (*Adjoint Transposed Convection*) term in equation (6) is nothing but the adjoint counterpart of the Newton term in equation (2) caused by the non-linearity, i.e. the discrepancy in between Oseen and full Newton linearization. As such it is a zeroth order term (*ATC-0* - which is preferable if to be treated explicitly) but it admits another popular 1st order form (*ATC-1*): $-(\nabla \boldsymbol{u}^*)\,\boldsymbol{u}$, which can easily be derived, adopting the following change of variables:

$$\left.\begin{aligned}u^* &\leftarrow u^* \\ \mathrm{p}^* &\leftarrow \mathrm{p}^*+\left(u\cdot u^*\right)\end{aligned}\right\} \tag{12}$$

Finally it is worth mentioning that as a direct consequence of the *frozen turbulence* assumption, equations (4)-(5) do not have any adjoint counterpart.

Porous Media Adjoint

The presence of the porous media source term in equation (2) shall be reflected in the adjoint equations for a proper handling of the heat exchanger impact on the change of design induced flow modifications. Differentiation of the Darcy term in equation (1) is straightforward but the Forchheimer term requires a little bit more attention. Differentiating (1) we get:

$$\begin{aligned}\delta\left(\nabla p\right)_{porous} &= \left(\overline{\overline{A}}+\|u\|\overline{\overline{B}}\right)\delta u \;+\left(\delta\|u\|\right)\left(\overline{\overline{B}}\,u\right) \\ &= \left(\overline{\overline{A}}+\|u\|\overline{\overline{B}}\right)\delta u \;+\frac{\left(u\cdot\delta u\right)}{\|u\|}\left(\overline{\overline{B}}\,u\right) \\ &= \left(\overline{\overline{A}}+\|u\|\overline{\overline{B}}+\frac{\left(\overline{\overline{B}}\,u\otimes u\right)}{\|u\|}\right)\delta u\end{aligned} \tag{13}$$

And finally we have:

$$\left(\nabla p^*\right)_{porous} = \left(\overline{\overline{A}}^T+\|u\|\overline{\overline{B}}^T+\frac{\left(u\otimes\overline{\overline{B}}\,u\right)}{\|u\|}\right)u^* \tag{14}$$

Which needs to be added as a source term to the left-hand side of equation (6) to account correctly for porous media effect.

Choice of Design Strategy

Due to the hidden nature of the underhood (see Figure 1) it makes sense to prefer topology over shape optimization as it allows for more creativity (richer design space) in the exploration of the optimal shapes. In our model problem (see Figure 2) the region to optimize Ω_{topo} is marked with a textured background.

Following [8] we intend to shape this space by finding optimal (artificial) Darcy coefficients k and make decision where to fill based on the criterion:

$$k \geq k_0 \tag{15}$$

With k_0 some big enough threshold. How to choose this threshold and attract the porosity coefficient towards either very low or very high values (*black/white topologies*) is a sensitive topic and goes beyond the scope of this work but the interested reader may refer to [7].

According to this methodology, some artificial Darcy term is introduced in both primal and adjoint momentum equations:

$$\begin{aligned}\mathbb{R}_u = \nabla\cdot\left(u\otimes u\right)+\nabla\cdot\left(-\left(\nu+\nu_t\right)\left(\nabla u+\nabla^T u\right)\right)+\nabla \mathrm{p} \\ +\left(\nabla p\right)_{porous}\;\mathbf{1}_{H_X}\;+k\,u\,\mathbf{1}_{\Omega_{topo}}=\mathbf{0}\end{aligned} \tag{16}$$

$$\mathbb{R}_{u^*} = -\nabla\cdot\left(u^*\otimes u\right)+\nabla\cdot\left(-\left(\nu+\nu_t\right)\left(\nabla u^*+\nabla^T u^*\right)\right) \tag{17}$$

$$+\nabla \mathrm{p}^*+\underbrace{\left(\nabla u\right)\;u^*}_{ATC\,2}+\left(\frac{\partial g}{\partial u}\right)^T$$

$$+\left(\nabla p^*\right)_{porous}\;\mathbf{1}_{H_X}+k\,u^*\;\mathbf{1}_{\Omega_{topo}}=\mathbf{0}$$

And the sensitivity is computed though:

$$\frac{dF}{dk}=\left(u\cdot u^*\right)\mathbf{1}_{\Omega_{topo}} \tag{18}$$

Such a design strategy however comes with a challenge with respect to the drag minimization. Indeed, not only does the fuzzy nature of the extracted solid boundary (high sensitivity to the thresholding value $\boldsymbol{k_0}$ in (15)) makes it difficult to compute the aerodynamic force integral over it but even in the case of sharp coefficients (black-white topology) this is likely to be the region where most numerical errors concentrate due to the induced pressure jump (see by example [9] for a discussion on this topic). For these reasons it seems inadequate to resort to classical drag force computation and use associated cost function. This has motivated the implementation of an alternative computation, that we call *indirect force*, as described in the next section.

Indirect Drag Force Cost Function

Formulation Classically the drag force exerted by a flow on a collection of immersed bodies (as in our model problem -see Figure 2) and through some porous media H_x is expressed as:

$$F_{drag} = \int_{H_x}\left(\nabla p\right)_{porous}\cdot d+\sum_{bodies}\int_{\partial\Omega_{\mathrm{body}}}\tau_n\cdot d \tag{19}$$

Where $\boldsymbol{d}$ is the direction of the incoming flow.

© 2018 SAE International; General Motors LLC.

Using the momentum equilibrium however it is possible to derive an alternative formulation of this force. Indeed, projecting (2) along the direction $\boldsymbol{d}$ and integrating over the domain yields:

$$\int_\Omega \mathbb{R}_u \cdot \boldsymbol{d} = 0 = \left\{ \int_\Omega \nabla\cdot(\boldsymbol{u}\otimes\boldsymbol{u}) + \nabla\cdot\left(-(\nu+\nu_t)\left(\nabla\boldsymbol{u}+\nabla^T\boldsymbol{u}\right)\right) + \nabla p \right\}\cdot\boldsymbol{d} + \int_{H_x} (\nabla p)_{porous}\cdot\boldsymbol{d} \quad (20)$$

Then, applying Green-Gauss formula we get:

$$\int_{\mathrm{H_x}} (\nabla \mathrm{p})_{porous}\cdot\boldsymbol{d} + \sum_{bodies}\int_{\partial\Omega_{\mathrm{body}}} \tau_n\cdot\boldsymbol{d} = -\int_{In\bigcup Ww} \tau_n\cdot\boldsymbol{d} - \int_{Out}(\boldsymbol{u}\cdot\boldsymbol{n})(\boldsymbol{u}\cdot\boldsymbol{d}) \quad (21)$$

Where *In*, *Out* and *Ww* denote the inlet, outlet and wind tunnel walls, respectively. Identity (21) then justifies the definition of

$$F_{drag}^{indirect} = -\int_{In\bigcup Ww} \tau_n\cdot\boldsymbol{d} - \int_{Out}(\boldsymbol{u}\cdot\boldsymbol{n})(\boldsymbol{u}\cdot\boldsymbol{d}) \quad (22)$$

as it is formally equivalent to $\boldsymbol{F_{drag}}$. Moreover, this formulation has the merit to imply only boundary integrals over the inlet, outlet and wind tunnel walls, which are all far away from the topological zone $\boldsymbol{\Omega_{topo}}$, hence circumventing the issues outlined in the former section.

It is worth mentioning that this alternative drag formulation has already been pointed out in [10], however in a different context and for different purposes.

Associated adjoint boundary conditions may easily be derived using (11), and we arrive at the following equations:

$$\left.\begin{array}{ll} outlet: & \tau_n^* = (\boldsymbol{u}^*-\boldsymbol{d})(\boldsymbol{u}\cdot\boldsymbol{n}) - \boldsymbol{n}(\boldsymbol{u}\cdot\boldsymbol{d}) \\ inlet + wind\ tunnel\ walls: & \boldsymbol{u}^* = \boldsymbol{d} \\ bodies\ walls: & \boldsymbol{u}^* = \boldsymbol{0} \end{array}\right\} \quad (23)$$

Link with Direct Drag Cost Function The conditions (23) have to be compared with the classical non porous *direct drag force* adjoint boundary conditions (see eg [2]):

$$\left.\begin{array}{ll} outlet: & \tau_n^* = \boldsymbol{u}^*(\boldsymbol{u}\cdot\boldsymbol{n}) \\ inlet + wind\ tunnel\ walls: & \boldsymbol{u}^* = \boldsymbol{0} \\ bodies\ walls: & \boldsymbol{u}^* = -\boldsymbol{d} \end{array}\right\} \quad (24)$$

Applying now following change of variables to the indirect force adjoint:

$$\left.\begin{array}{l} \tilde{\boldsymbol{u}}_{ind}^* \leftarrow \boldsymbol{u}_{ind}^* - \boldsymbol{d} \\ \tilde{\mathrm{p}}_{\mathrm{ind}}^* \leftarrow \mathrm{p}_{\mathrm{ind}}^* + (\boldsymbol{u}\cdot\boldsymbol{d}) \end{array}\right\} \quad (25)$$

It is easy to see that, $\left(\tilde{\boldsymbol{u}}_{ind}^*, \tilde{\mathrm{p}}_{\mathrm{ind}}^*\right)$ do obey the same equations than the direct force adjoint $\left(\boldsymbol{u}_{dir}^*, \mathrm{p}_{\mathrm{dir}}^*\right)$. Indeed, substituting (25) in (23) yields:

$$\left.\begin{array}{ll} outlet: & \tilde{\tau}_n^* = \tilde{\boldsymbol{u}}_{ind}^*(\boldsymbol{u}\cdot\boldsymbol{n}) \\ inlet + wind\ tunnel\ walls: & \tilde{\boldsymbol{u}}_{ind}^* = \boldsymbol{0} \\ bodies\ walls: & \tilde{\boldsymbol{u}}_{ind}^* = -\boldsymbol{d} \end{array}\right\}$$

Which is same as (24). Moreover, substituting in equation (6), we get:

$$\mathbb{R}_{u^*} = -\nabla\cdot\left(\tilde{\boldsymbol{u}}_{ind}^*\otimes\boldsymbol{u}\right) + \nabla\cdot\left(-(\nu+\nu_t)\left(\nabla\tilde{\boldsymbol{u}}_{ind}^* + \nabla^T\tilde{\boldsymbol{u}}_{ind}^*\right)\right) + \nabla\left(\tilde{\mathrm{p}}_{\mathrm{ind}}^* - (\boldsymbol{u}\cdot\boldsymbol{d})\right) + (\nabla\boldsymbol{u})\ (\tilde{\boldsymbol{u}}^* + \boldsymbol{d}) + \left(\frac{\partial g}{\partial \boldsymbol{u}}\right)^T = \boldsymbol{0}$$

And then, as claimed:

$$\mathbb{R}_{u^*} = -\nabla\cdot\left(\tilde{\boldsymbol{u}}_{ind}^*\otimes\boldsymbol{u}\right) + \nabla\cdot\left(-(\nu+\nu_t)\left(\nabla\tilde{\boldsymbol{u}}_{ind}^* + \nabla^T\tilde{\boldsymbol{u}}_{ind}^*\right)\right) + \nabla\tilde{\mathrm{p}}_{\mathrm{ind}}^* + (\nabla\boldsymbol{u})\ \tilde{\boldsymbol{u}}^* + \left(\frac{\partial g}{\partial \boldsymbol{u}}\right)^T = \boldsymbol{0}$$

Finally, the continuity equation is not affected by a uniform shift. An immediate corollary is that:

$$\left.\begin{array}{l} \boldsymbol{u}_{dir}^* = \boldsymbol{u}_{ind}^* - \boldsymbol{d} \\ \mathrm{p}_{\mathrm{dir}}^* = \mathrm{p}_{\mathrm{ind}}^* + (\boldsymbol{u}\cdot\boldsymbol{d}) \end{array}\right\} \quad (26)$$

As a consequence, the shape sensitivity vector on the bodies, which may be expressed as (see e.g. [8] for details):

$$G = -(\nu+\nu_t)(\partial_n\boldsymbol{u})(\partial_n\boldsymbol{u}^*) \quad (27)$$

Remains unchanged when switching from direct to indirect force formulation, and consistency is ensured.

Validation To validate the approach, let us consider the simple case of a 2D flow over an airfoil (see Figure 3 for the velocity profile).

One would like first to confirm the agreement of the indirect force cost function versus a direct computation (see Figure 4). According to formula (22) one expects both values to agree once steady-state has been reached.

Next, we are interested in validating the result of equations (26) about the relationship in between *direct force* and *indirect force* adjoints. To do so, a first computation is run with the cost function set as *direct force* and a second one with the cost function set as *indirect force*. Then we plot the discrepancy magnitude of the 2 adjoint velocities (see Figure 5).

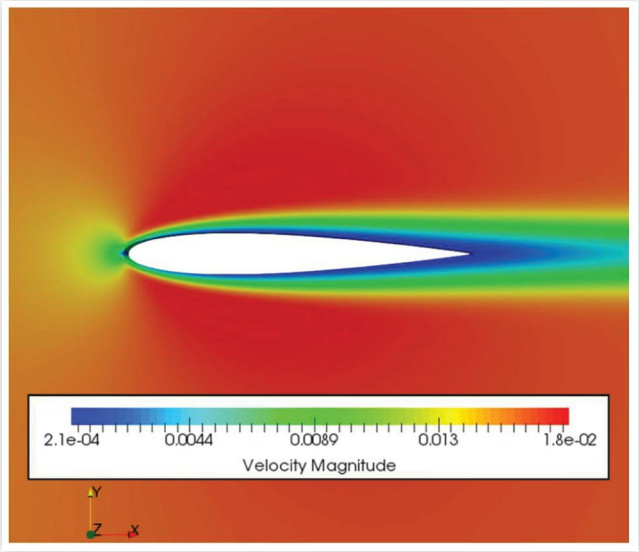
According to (26) one should have:

$$\left\|\boldsymbol{u}_{dir}^* - \boldsymbol{u}_{ind}^*\right\| = \|\boldsymbol{d}\| = 1 \quad (28)$$

Everywhere in the domain, which is indeed in good agreement with contour plot shown in Figure 5.

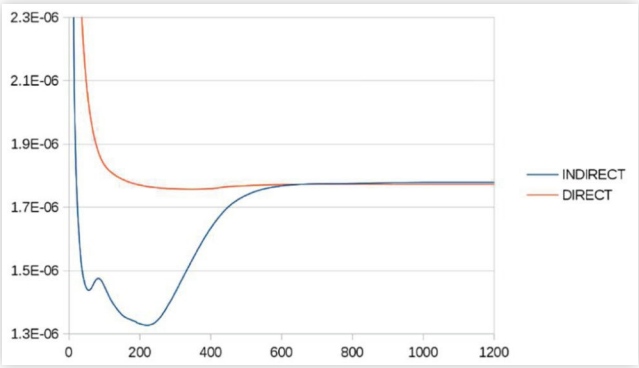
© 2018 SAE International; General Motors LLC.

FIGURE 3 Velocity profile of the flow around the airfoil. Reynolds number is around 1000.



© SAE International

FIGURE 4 Red curve shows the convergence history of the direct drag force whereas the blue one corresponds to the indirect force. We can observe that both converge to very close values even if it takes longer time for the indirect force to converge, which is due to the fact that the flow needs to be converged everywhere in the domain for both values to agree.



© SAE International

Volumetric Flow Rate Cost Function

Formulation The cooling effect of the flow on the heat exchanger may be related to the quantity of air that flows through it. Hence the quantity:

$$\dot{V} = \int_{H_x} \boldsymbol{u} \cdot \boldsymbol{d} \tag{29}$$

Known as the *volumetric flow rate* may be regarded as a good measure of this effect. It is worth mentioning that this integral is free from leakage flow as the support domain only covers the heat exchanger. As we are interested in maximizing this quantity, the sign has to be reverted in order to fit in the classical minimization framework and for this reason one shall consider the following cost function:

$$\dot{V}' = -\int_{H_x} \boldsymbol{u} \cdot \boldsymbol{d} \tag{30}$$

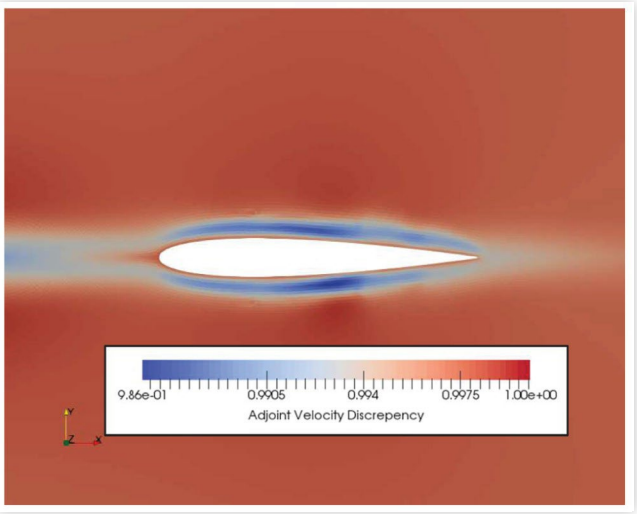
As this is a volumetric cost function it does not add any source term to the adjoint boundary conditions and they simply read:

$$\left.\begin{aligned} outlet: \quad & \tau_n^* = \boldsymbol{u}^* (\boldsymbol{u} \cdot \boldsymbol{n}) \\ inlet + walls: \quad & \boldsymbol{u}^* = \boldsymbol{0} \end{aligned}\right\} \tag{31}$$

The volumetric adjoint momentum source term $\left(\frac{\partial g}{\partial \boldsymbol{u}}\right)^T$, on the other hand, is no longer zero and may easily be computed to:

$$\left(\frac{\partial g}{\partial \boldsymbol{u}}\right)^T = -\boldsymbol{d}\ \mathbf{1}_{H_X} \tag{32}$$

FIGURE 5 the contour represents the magnitude of $\left(\boldsymbol{u}_{dir}^* - \boldsymbol{u}_{ind}^*\right)$ which is expected to be one everywhere, according to (26). The agreement is indeed fairly reasonable in this case.



© SAE International

Simulation Examples To illustrate the consistency of this new cost function, one considers the case of a collection of bluff bodies positioned in front of a porous media (see Figure 6 and Figure 7).

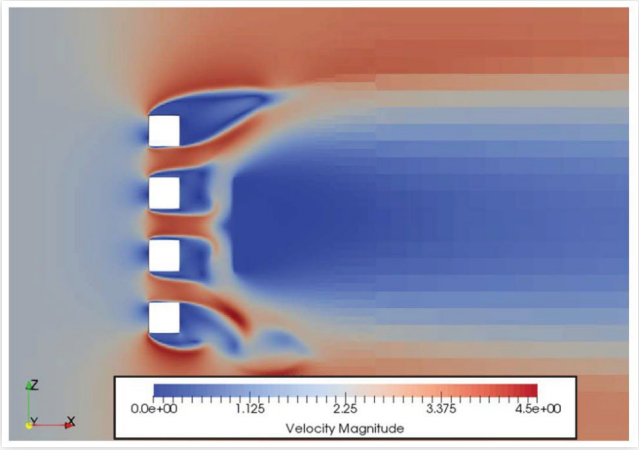
Optimization strategy

Statement of the Problem

One promising way to balance engine cooling with front-end drag force is through the usage of an advanced technology known under the name Active Grille Shutter system, which

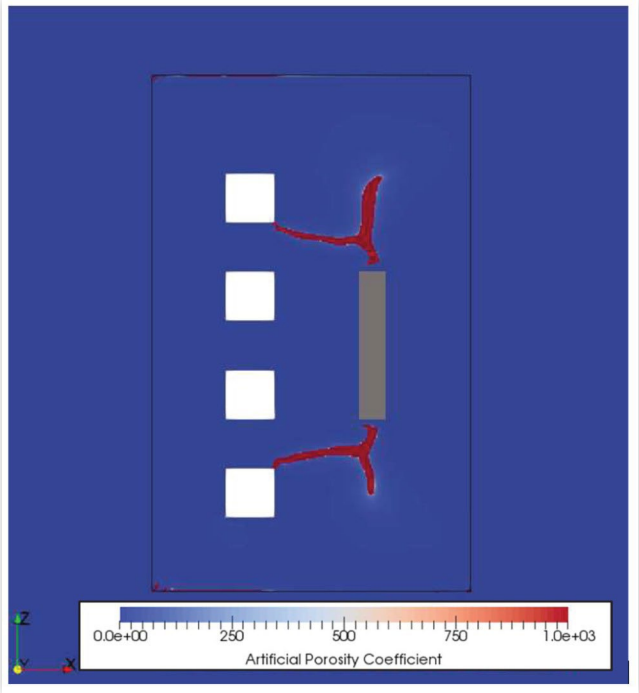
© 2018 SAE International; General Motors LLC.

FIGURE 6 Flow around a collection of bluff bodies with a porous media positioned at the rear. Configuration is slightly asymmetric as the bluff bodies row is closer from the lower symmetry plane than from the upper one.



© SAE International

FIGURE 7 The artificial Darcy coefficient is represented. The black lines delimit the topological zone. One can observe that there is a tendency to concentrate the flow towards the porous media (in grey color, at the rear) with the creation of 2 T-shaped branches at the top and bottom of it. Also, as it might have the side effect to divert the flow before it goes through the bluff bodies, the 2 slim fingers at top and bottom left of the box might be understood as an attempt to counteract this phenomenon.



© SAE International

opens and closes the grille dynamically, as proposed by a few car manufacturers such as General Motors. It has been reported in [15] that efficient control algorithms may be designed in order to actively tune the airflow through heat exchanger module, so that a fuel economy up to 2.6% is achieved.

Alternatively, or complementarily, one might be interested in selecting an efficient frontend design. It is indeed reasonable to expect that an optimized shape may provide less penalty for the body drag for the same amount of cooling flow increase.

In this approach, one would like to address combined optimization of drag force, in order to maximize the aerodynamic efficiency of the vehicle, and volumetric flow rate so that the cooling effect is improved as well. Unfortunately, this is somewhat contradictory in the terms as these two objectives happen to be naturally in competition. Indeed, decomposing the drag force (19):

$$F_{drag} = \underbrace{\int_{H_x} (\nabla p)_{porous} \cdot d}_{porous\ drag} + \underbrace{\sum_{bodies} \int_{\partial\Omega_{body}} \tau_n \cdot d}_{body\ drag} \tag{33}$$

We can easily see that the porous drag component shall naturally increase when the volumetric flow rate (29) is improved. More specifically, we have:

$$\begin{aligned} \int_{H_x} (\nabla p)_{porous} \cdot d &= \int_{H_x} \left\{ \left(\overline{\overline{A}} + \|u\| \overline{\overline{B}} \right) u \right\} \cdot d \\ &= \int_{H_x} u \cdot \left\{ \left(\overline{\overline{A}}^T + \|u\| \overline{\overline{B}}^T \right) d \right\} \end{aligned} \tag{34}$$

Making now the reasonable assumptions that the dominant directions of $\overline{\overline{A}}$ and $\overline{\overline{B}}$ are aligned with the incoming flow direction $\boldsymbol{d}$ and so is the flow within the heat exchanger $\boldsymbol{H_x}$, which moreover is almost uniform, we can state that:

$$\begin{aligned} \int_{H_x} (\nabla p)_{porous} \cdot d &\approx \left(\left\| \overline{\overline{A}} \right\| + \frac{\int_{H_x} u \cdot d}{|H_x|} \left\| \overline{\overline{B}} \right\| \right) \int_{H_x} u \cdot d \\ &\approx \left(\left\| \overline{\overline{A}} \right\| + \frac{\dot{V}}{|H_x|} \left\| \overline{\overline{B}} \right\| \right) \dot{V} \end{aligned} \tag{35}$$

Where $|H_x|$ denotes the heat exchanger volume. We can observe then that this is an increasing function of the *volumetric flow rate*.

For this reason, one shall only consider the non-porous drag component in our optimization set-up. According to (22) this might be formulated indirectly as:

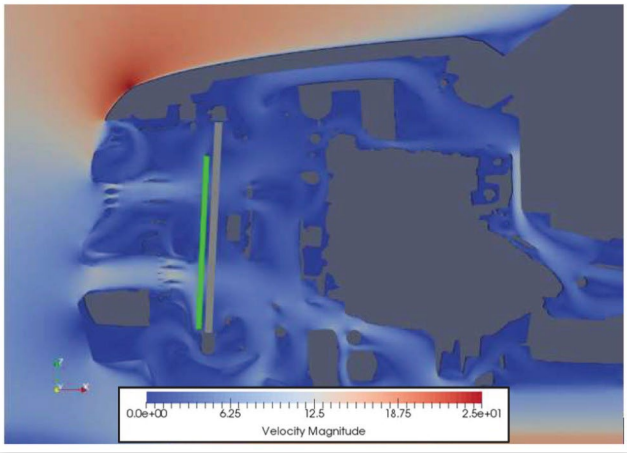
$$\begin{aligned} F^{indirect}_{body\ drag} &= -\int_{In \cup Ww} \tau_n \cdot d - \int_{Out} (u \cdot n)(u \cdot d) \\ &\quad - \int_{H_x} (\nabla p)_{porous} \cdot d \end{aligned} \tag{36}$$

Or approximately, using the *volumetric flow rate* and *indirect drag force* cost functions together with equation (35).

The effect of considering only the non-porous drag may be outlined by considering the case of a flow in a 2D slice of the underhood of the pick-up truck (see Figure 8 and Figure 9).

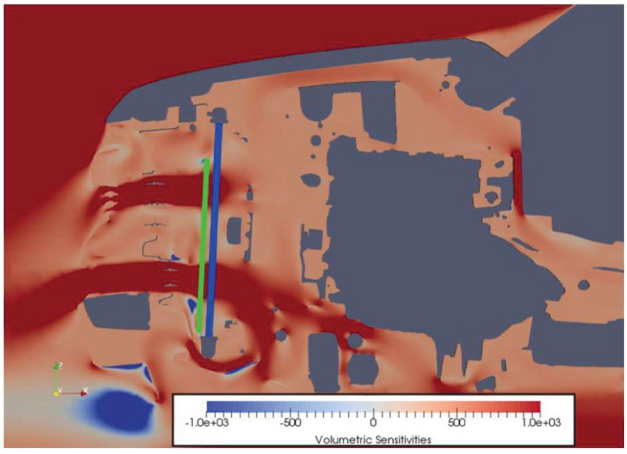
© 2018 SAE International; General Motors LLC.

FIGURE 8 Green and grey bars represent the condenser and heat exchanger, respectively. One can observe just in front of the condenser, at its very bottom, that some flow here tries to escape from beneath, which results in body drag increase.



© SAE International

FIGURE 9 Volumetric sensitivities of body force cost function (i.e. indirect drag force lest heat exchanger porous drag). The small blue island close to the bottom left of the condenser can be interpreted as an attempt to counteract the flow diversion observed in Figure 8. This would have not been possible if we had considered the total indirect force as blocking those cells results in an increase flow through the condenser, hence an increased porous drag.



© SAE International

It is worth mentioning that, although some significant secondary flow might be observed in the engine compartment, no special boundary condition has been set to air cool other vehicle components. Some of this flow may be necessary in particular cases, however it is not an area of interest for this study, which simply looks at obtaining a maximum flow rate through the heat exchangers whilst minimizing drag of the vehicle. It could well be the subject of a future study.

Choice of an Optimization Framework

One possibility would be to treat the problem as a single objective optimization under constraints:

$$\left.\begin{array}{l} ! F_{body\ drag}^{indirect} \\ s.t. \dot{V} \geq \dot{V}_0 \end{array}\right\} \tag{37}$$

And use some kind of penalization method to handle the constraint or the finer-grained augmented lagrangian approach (see eg [11]). But this does not fit exactly our purpose.

Indeed, in order to reach acceptable optimum in term of performance from one side and constraint satisfaction, from the other side, this family of methods usually perform outer loops on the sensitive so-called *penalization parameter* γ_n, solving approximately at each step an auxiliary optimization problem:

$$! F_{body\ drag}^{indirect} + \gamma_n * g\left(\dot{V} - \dot{V}_0\right)$$

which, on one hand might be tedious and time consuming in the context of industrial CFD simulations, and on the other hand require very robust optimization solvers in order to handle all these intermediate steps without exiting prematurely with an unsatisfying solution.

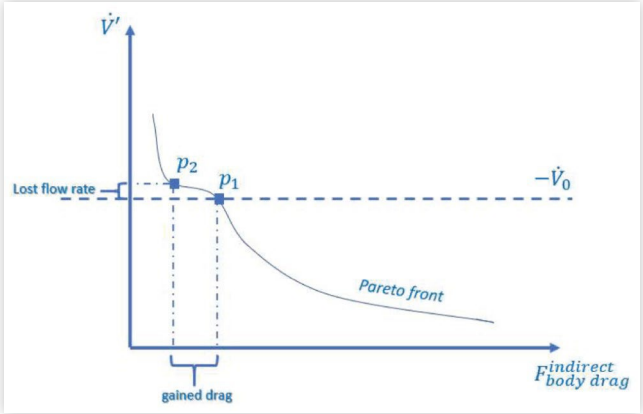
Another reason is that, to some extent, one would like to explore the Pareto front (see [12] for details) and decide *a posteriori* what is the best fit for our purpose, as exemplified in Figure 10.

For these reasons we prefer to adopt a multi-objective optimization framework, trying to optimize both objectives *at the same time* and find some interesting points on the Pareto front.

Multi-Objective Optimization

One of the most widely used method for multi-objective optimization is the *weighted sum method* (see [12] for reference). This method transforms multiple objectives into an

FIGURE 10 p_1 is the optimum of the minimization problem under constraint, but depending on the context, one might in fact prefer p_2 over p_1 as it allows to gain substantial drag counts whilst only sacrificing a small amount of cooling.



© SAE International

© 2018 SAE International; General Motors LLC.

aggregated scalar objective function (hence the name *scalarization* used by some authors) by multiplying each objective function by a weighting factor and summing up all contributors, which in our bi-objective context would lead to:

$$F = \omega_1 * F^{indirect}_{body\ drag} + (1-\omega_1) * \dot{V} \tag{38}$$

With $\omega_1 \in [0,1]$. Although quite simple and intuitive, this approach, however, suffers from several drawbacks, as described in [12]. First of all, the selection of an appropriate weight is not easy and somewhat artificial, and furthermore the method is known to miss all the points in the concave region of the Pareto front (everything in between $p_1$and p_2 in the example of Figure 10) whatever the weights, as well as to yield non-uniform sampling of the convex part, with an accumulation near the inflection points.

An interesting alternative to *the weighted sum approach* is provided in [13], where the *Multiple Gradient Descent Algorithm (MGDA)* is introduced. The idea is, at each step, to seek for a direction d, which is a descent direction for all the objectives. More specifically, d is chosen as the *minimal norm elemen*t within the objective function gradients convex set:

$$\mathcal{C} = \left\{ \mathbb{d} \in \mathbb{R}^n / \mathbb{d} = \sum_{i=1..n} \omega_i \nabla F_i ;\ \omega_i \geq 0\ (\forall i);\ \sum_{i=1..n} \omega_i = 1 \right\} \tag{39}$$

The *minimal norm element* is proven to be either a descent direction for all objectives F_i or zero, in which case some point on the (weak) Pareto front has been reached. It is worth mentioning at this stage that, although the descent direction d is expressed as a convex combination of the objective function gradients as in the weighted sum method, the weights here are not constant throughout the iterations: they depend on the objective functions gradients themselves and change at each step. This does have a major consequence in the context of adjoint-based optimization as it implies to solve an adjoint system for each cost function independently, contrarily to the standard *weighted sum approach* where only one adjoint system has to be solved for the combined objective. This is a price to pay to allow for more flexibility in the solving of the multi-objective optimization problem.

Despite its merits, the *MGDA* does not fit our purpose entirely as it makes no distinction in between objectives and does not favor any one on the other. In our case, however, there is a clear preference for drag reduction. The volumetric flow rate is more like a constraint: we would like to reach a minimal amount and we are not against a little extra provided it hardly impacts the drag. This motivates the derivation of an alternative approach, hereafter called *Optimize Both Favor One (OBFO)*, as detailed in the next section.

Optimize Both Favor One

In this approach, emphasis is put on one of the cost function, F_1,that is called *principal*, whereas the second one F_2 is deemed *secondary*.

At each step of the optimization process we seek for a unit direction d that is locally the optimal descent direction for F_1 under the constraint that it does not increase F_2.

This can be formulated as follows:

$$\left.\begin{array}{l} d = \underset{\mathbb{d}/\|\mathbb{d}\|=1}{\operatorname{argmin}} (\nabla F_1 \cdot \mathbb{d}) \\ s.t.\quad \nabla F_2 \cdot \mathbb{d} \leq 0 \end{array}\right\} \tag{40}$$

We say that $F_1$is favoured over F_2 in the sense that we aim at decreasing F_1 as much as possible, whereas for F_2 it is less stringent as the only requirement is to not increase it.

The solution of (40) may be computed explicitly using KKT theory:

$$\left.\begin{array}{l} d = -\dfrac{\nabla F_1}{\|\nabla F_1\|} \text{ if } \|\nabla F_2\| = 0 \text{ or } q \in [0,1] \\ d = -\dfrac{\nabla F_1}{\|\nabla F_1\|\sqrt{1-q^2}} + \dfrac{q\,\nabla F_2}{\|\nabla F_2\|\sqrt{1-q^2}} \text{ if } q \in]-1,0[\end{array}\right\} \tag{41}$$

Where $q = \dfrac{\nabla F_1 \cdot \nabla F_2}{\|\nabla F_1\|\|\nabla F_2\|} \in [-1,1]$ is the Cauchy-Schwarz quotient (cosine of the angle in between ∇F_1 and ∇F_2).

There are 2 degenerate cases: the first one corresponds to $\|\nabla F_1\| = 0$ in which case a local optimum has been reached for F_1, the second one happens when ∇F_1 and ∇F_2 are in opposite direction ($q = -1$), in which case some point in the (weak) Pareto front has been reached.

A slight generalization of the above, hereafter called *OBFO(α)* is to replace the constraint $\nabla F_2 \cdot \mathbb{d} \leq 0$ in (40) by a condition of minimal alignment: $\nabla F_2 \cdot \mathbb{d} \leq -\alpha \|\nabla F_2\|$ $\alpha \in [0,1[$, leading to:

$$\left.\begin{array}{l} d = -\dfrac{\nabla F_1}{\|\nabla F_1\|} \text{ if } \|\nabla F_2\| = 0 \text{ or } q \in [\alpha,1] \\ d = \dfrac{-\sqrt{1-\alpha^2}\,\nabla F_1}{\|\nabla F_1\|\sqrt{1-q^2}} + \dfrac{\left(q\sqrt{1-\alpha^2} - \alpha\sqrt{1-q^2}\right)\nabla F_2}{\|\nabla F_2\|\sqrt{1-q^2}} \\ \text{if } q \in]-1,\alpha[\end{array}\right\} \tag{42}$$

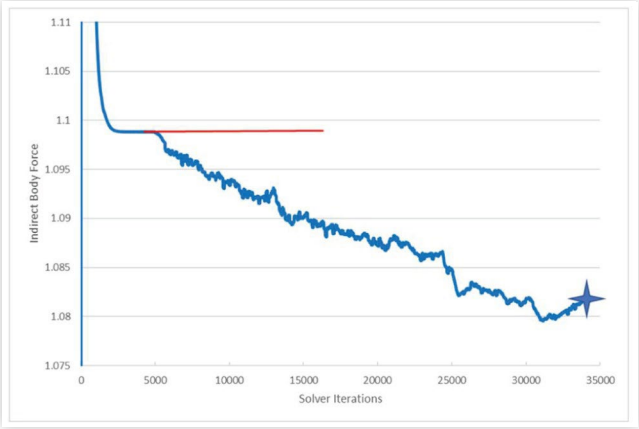
It is advised to introduce at least a small safety factor α, especially when there is some uncertainty in the gradient computations, so that to ensure an effective decrease in F_2.

For the previously mentioned pick-up truck case, the simple *weighted sum method* is ineffective. Not only does the process fail after multiple attempts because of the requirement for dynamic blending, but also finding a satisfying blending factor between the two cost function gradients results in a time-consuming trial and error process. On the contrary, the *OBFO(α = 20%)* is straightforward to setup, does not require tuning and was successfully applied as seen in Figure 11 and Figure 12.

The design was modified every 100 iteration of primal and adjoint solve, and terminated after 291 optimization cycles (i.e 29100 iteration). At the last cycle the OBFO algorithm was unable to find a direction which satisfied a minimum of 20% alignment for both objectives. The final design results in a 1.6% drag decrease and a 5.6% volumetric flow rate increase through both heat exchangers.

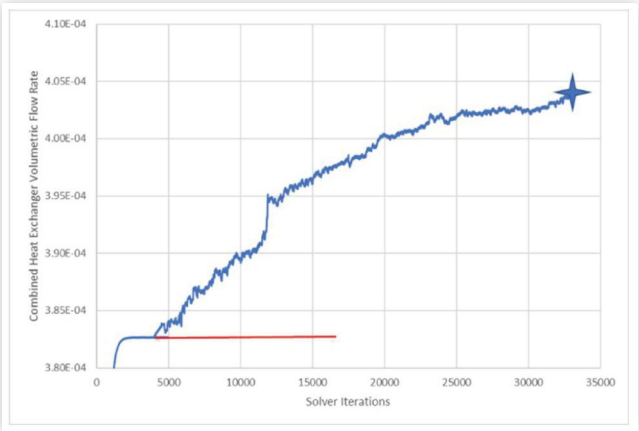
© 2018 SAE International; General Motors LLC.

FIGURE 11 Indirect body force cost function evolution of pick-up truck case using *OBFO(0.2)* strategy. Red line shows convergence level of the cost function before optimization starts.



© SAE International

FIGURE 12 Volumetric flow rate cost function evolution of pick-up truck case using *OBFO(0.2)* strategy. Red line shows convergence level of the cost function before optimization starts.



© SAE International

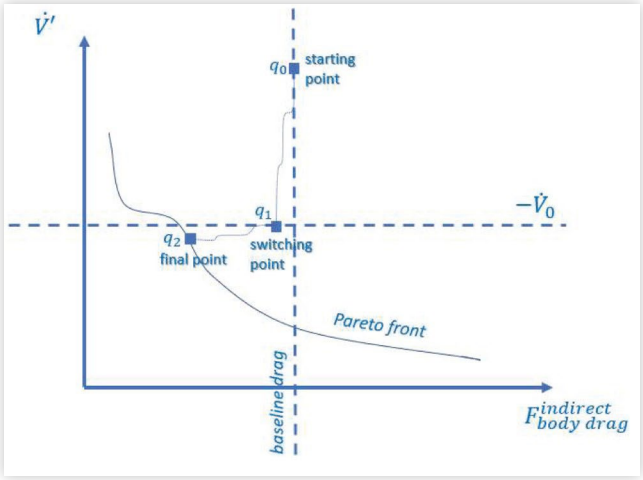
Switched OBFO with Revert Assist

Switching Focus Coming back to our combined drag force and cooling flow rate optimization problem, there are 2 different scenarios to consider. The first one corresponds to the case where we do have enough cooling effect already ($\dot{V} \geq \dot{V}_0$), whereas in the second one minimal flow rate Fr_0 has not been reached yet.

In the first case, it is reasonable to use *OBFO* with the drag force $F^{indirect}_{body\ drag}$ taken as the principal objective, whereas in the second case, on the contrary, we would like to reach the minimal cooling flow rate $\dot{V}_0$ as fast as possible without degrading the drag too much, which corresponds to using *OBFO* with V' as the principal objective.

Let us consider now the scenario illustrated in Figure 13 where we do start from a non-admissible point ($\dot{V} < \dot{V}_0$) and

FIGURE 13 During phase 1, $\dot{V}'$ is taken as the *principal objective* until the target minimal flow rate $\dot{V}_0$ is reached, then phase 2 starts at the switching point and $F^{indirect}_{body\ drag}$ becomes *the principal objective*.



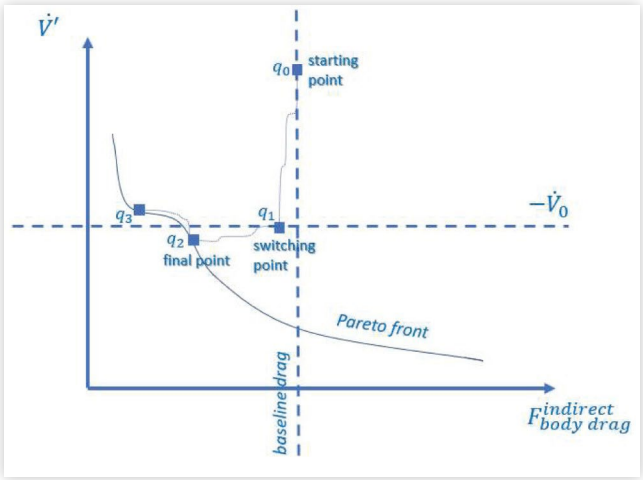
© SAE International

consequently apply *OBFO* with $\dot{V}'$ as the principal objective for several steps. Then, hopefully at some point, the minimal cooling flow rate shall be reached and the drag becomes the predominant objective. This motivates a switch from $\dot{V}'$ to $F^{indirect}_{body\ drag}$ as the principal objective in our *OBFO* algorithm.

Revert Assist In the former illustrative example (Figure 13) the optimization process stops at $q_2$which seems a fairly reasonable choice as it outperforms minimal cooling flowrate whilst achieving lower drag than baseline. If, however, it is acceptable to underperform slightly the maximal cooling flowrate, significant further improvement may be achieved on the drag.

Moving from q_2 to some better drag point, however, would require to start by increasing the cooling flow rate (hence the

FIGURE 14 Restarting from q_2 with modified *OBFO* strategy (43) allows to temporarily relax the non-increasing flow rate condition if the drag reduction promise is sufficient, then switching back to classical *OBFO* allows to converge towards q_3.



© SAE International

© 2018 SAE International; General Motors LLC.

name *revert assist*). This is of interest only if the drag reduction promise is significantly greater than the corresponding cooling flow rate decrease. More specifically, if this reduction vs increase ratio is quantified to some value $\mathbb{r}$, then it makes sense to modify the initial *OBFO* problem (40) in the following way:

$$\left.\begin{array}{c} d = \underset{\frac{\mathbb{d}}{\|\mathbb{d}\|}=1}{\operatorname{argmin}}(\nabla F_1 \cdot \mathbb{d}) \\ s.t. \quad \nabla F_2 \cdot \mathbb{d} \leq -\mathbb{r}\ \nabla F_1 \cdot \mathbb{d} \end{array}\right\} \tag{43}$$

Depending on the value of $\mathbb{r}$ and the magnitude of ∇F_1 some feasible direction d might exist or not at the restart point q_2. Repeating this process a couple of steps and then switching back to the former *OBFO* strategy with $F_{body\ drag}^{indirect}$ taken as the principal objective, might allow to discover some point on the cooling flow rate plateau as exemplified in Figure 14.

Summary/Conclusions

A framework has been introduced to address combined optimization of cooling flow rate and drag force on road vehicles. To do so, 2 new cost functions have been implemented:

- *Indirect force* (with or without porous drag in it): this is formally equivalent to the *direct force* computation but allows to perform topology drag optimization, as cost function support lies far away from the topological zone, contrarily to the *direct force* approach.
- *Volumetric flow rate through the heat exchanger*: this is a standard measure of the cooling effect, hence a good criterion to optimize for.

The adjoint of the heat exchanger model based on the Darcy-Forchheimer formulation for porous media was derived and implemented.

Also, a new multi-objective strategy, called *Optimize Both Favor One* (*OBFO*) has been presented, which offers more flexibility than *weighted sum approach* and *MGDA* in the research of an adequate Pareto point, depending on the fine-grained user objective.

Some preliminary validation cases have been presented. Active current work involves application of this methodology to a greater number of road vehicles in order to demonstrate the full potential of this framework.

References

1. http://www.iconcfd.com, November 2017
2. Schmidt S., Schulz V., "Shape Derivatives for General objective Functions and the Incompressible Navier-Stokes Equations," *Control and Cybernetics*, vol. 39 (2010), N° 3.
3. Bear J., "*Dynamics of Fluids in Porous Materials*," American Elsevier, 1972. Also reissued by Dover publication, 1988.
4. Nadarajah, S., Jameson A., "Studies of the Continuous and Discrete Adjoint Approaches to Viscous Automatic Aerodynamic Shape Optimization," *15th AIAA Computational Fluid Dynamics Conference*, Anaheim, CA.
5. Popovac M., Reichl C, Jasak H., Rusche H., "RANS Turbulence Treatment for Continuous Adjoint Optimization," *8th International Symposium on Turbulence, Heat and Mass Transfer 8*, Sarajevo, Bosnia and Herzegovina.
6. Hinterberger C., Olesen M., "Industrial Applications of Continuous Adjoint Flow Solvers for the Optimization of Automotive Exhaust System," *CFD & Optimization, 2011-069 An ECCOMAS Thematic Conference*, 23-25 May 2011, Antalya, Turkey.
7. Deaton, J. and Grandhi, R., "A Survey of Structural and Multidisciplinary Continuum Topology Optimization: Post 2000," *Struct Multidisc Optim* 49:1-38, 2014, doi:10.1007/s00158-013-0956-z.
8. Othmer, C., "A Continuous Adjoint Formulation for the Computation of Topological and Surface Sensitivities of Ducted Flows," *International Journal for Numerical Methods in Fluids* 58(8):861877, 2008.
9. Ramiere I., Angot P., Belliard M., "A general fictitious method with immersed jumps and multilevel nested structured meshes", *Journal of Computational Physics* 225, 2 (2007) pp 1347-1387" DOI : 10.1016/j.jcp.2007.01.026d.
10. Stuck, A., "Adjoint Navier-Stokes Methods for Hydrodynamic Shape Optimisation", PhD thesis, Techn. Univ., Hamburg-Harburg, 2011.
11. Arora, J.S., Chahande, A.I., and Paeng, J.K., "Multiplier Methods for Engineering Optimization," *International Journal for Numerical Methods in Engineering* 32(7):1485-1525, 1991, doi:10.1002/nme.1620320706.
12. Kim, I. and de Weck, O.L., "Adaptive Weighted Sum Method for Multiobjective Optimization: A New Method for Pareto Front generation," *Struct Multidisc Optim* 31:105-116, 2006, doi:10.1007/s00158-005-0557-6.
13. Desideri J.-A., "Multiple-Gradient Descent Algorithm (MGDA) for Pareto-Front Identification," In Fitzgibbon, W.; Kuznetsov, Y.A.; Neittaanmæki, P.; Pironneau, O. *Modeling, Simulation and Optimization for Science and Technology*, 34, Springer, 2014, Computational Methods in Applied Sciences, 978-94-017-9054-3. <hal-01096049>.
14. Othmer, C., "Adjoint Methods for Car Aerodynamics," *Journal of Mathematics in Industry* 4:6, 2014.
15. Mustafa, R., Schulze, M., Elits, P., and Kucukay, F., "Improved energy management using engine compartment encapsulation and grille shutter control," *SAE Int. J. Fuels Lubr.* 5(2):803-812, 2012, doi:10.4271/2012-01-1203.

All rights reserved. No part of this publication may be reproduced, stored in a retrieval system, or transmitted, in any form or by any means, electronic, mechanical, photocopying, recording, or otherwise, without the prior written permission of the copyright holder.

Positions and opinions advanced in this paper are those of the author(s) and not necessarily those of SAE International. The author is solely responsible for the content of the paper.

ISSN 0148-7191